remote sensing

MDPI

Article

Evaluating the Impact of Interferogram Networks on the Performance of Phase Linking Methods

Saeed Haji Safari [1] and Yasser Maghsoudi [2,*]

[1] Department of Photogrammetry and Remote Sensing, Faculty of Geodesy and Geomatics Engineering, K. N. Toosi University of Technology, Tehran 19967-15433, Iran; saeedsafari@email.kntu.ac.ir
[2] Department of Earth and Environmental Sciences, University of Exeter, Penryn Campus, Penryn TR10 9FE, Cornwall, UK
* Correspondence: y.maghsoudi-mehrani@exeter.ac.uk

Abstract: In recent years, phase linking (PL) methods in radar time-series interferometry (TSI) have proven to be powerful tools in geodesy and remote sensing, enabling the precise monitoring of surface displacement and deformation. While these methods are typically designed to operate on a complete network of interferograms, generating such networks is often challenging in practice. For instance, in non-urban or vegetated regions, decorrelation effects lead to significant noise in long-term interferograms, which can degrade the time-series results if included. Additionally, practical issues such as gaps in satellite data, poor acquisitions, or systematic errors during interferogram generation can result in incomplete networks. Furthermore, pre-existing interferogram networks, such as those provided by systems like COMET-LiCSAR, often prioritize short temporal baselines due to the vast volume of data generated by satellites like Sentinel-1. As a result, complete interferogram networks may not always be available. Given these challenges, it is critical to understand the applicability of PL methods on these incomplete networks. This study evaluated the performance of two PL methods, eigenvalue decomposition (EVD) and eigendecomposition-based maximum-likelihood estimator of interferometric phase (EMI), under various network configurations including short temporal baselines, randomly sparsified networks, and networks where low-coherence interferograms have been removed. Using two sets of simulated data, the impact of different network structures on the accuracy and quality of the results was assessed. These patterns were then applied to real data for further comparison and analysis. The findings demonstrate that while both methods can be effectively used on short temporal baselines, their performance is highly sensitive to network sparsity and the noise introduced by low-coherence interferograms, requiring careful parameter tuning to achieve optimal results across different study areas.

Keywords: InSAR; interferometry; phase linking; remote sensing; interferogram network; Sentinel-1; SBAS; graph theory

check for updates

Citation: Haji Safari, S.; Maghsoudi, Y. Evaluating the Impact of Interferogram Networks on the Performance of Phase Linking Methods. *Remote Sens.* **2024**, *16*, 3954. https://doi.org/10.3390/rs16213954

Academic Editors: Antonio Miguel Ruiz Armenteros and Deodato Tapete

Received: 11 September 2024
Revised: 2 October 2024
Accepted: 4 October 2024
Published: 23 October 2024

Copyright: © 2024 by the authors. Licensee MDPI, Basel, Switzerland. This article is an open access article distributed under the terms and conditions of the Creative Commons Attribution (CC BY) license (https://creativecommons.org/licenses/by/4.0/).

1. Introduction

With the launch of the ERS-1 satellite in 1991, a new era for interferometric synthetic aperture radar (InSAR) began. This successful mission provided the remote sensing community with an extensive dataset and offered the opportunity for continuous and precise monitoring of the displacement and deformation of the Earth's surface. However, interferograms often show low coherence in non-urban areas, especially in studies that involve long temporal baselines. Additionally, to accurately analyze deformation rates and minimize the impact of atmospheric effects, relying on just one interferogram is not enough [1]. Due to this, since the late 1990s, several different methods have been introduced to analyze time-series stacks of interferograms [1–8]. While these methods often have a common framework, the differences in the details and the way they are distinctly implemented have an important impact on the final accuracy level of the resulting measurements. For a set of

N SLC images captured at different times over the same area, one would be able to create a network of $N(N-1)/2$ interferograms. However, depending on the processing approach used for TSI analysis, this network configuration may vary.

The earliest time-series methods in InSAR primarily focused on surface points with dominant scattering properties, which are most prevalent in urban environments. These specific points are capable of maintaining coherence in interferograms, even over long temporal baselines, making them highly reliable for time-series analysis. Due to this stability, they are referred to as persistent scatterers [7], or permanent scatterers [1,4] (PS), and the associated TSI methods that utilize these points are collectively known as persistent scatterer interferometry (PSI). PS points are characterized by a high signal-to-noise ratio (SNR), which allows PSI methods to bypass the need for any form of averaging or multilooking that might otherwise be required to enhance the data quality. This efficiency makes using a network of $N(N-1)/2$ interferograms unnecessary and highly redundant [5]. Instead, time-series processing can be carried out by utilizing $N-1$ interferograms. This is achieved by selecting one arbitrary epoch as the master image, while the remaining epochs are used as slaves, thereby creating a single-master interferogram network (Figure 1a). This approach simplifies the processing and ensures that the data maintain its precision, accuracy, and spatial resolution, which is essential for reliable deformation monitoring in urban areas.

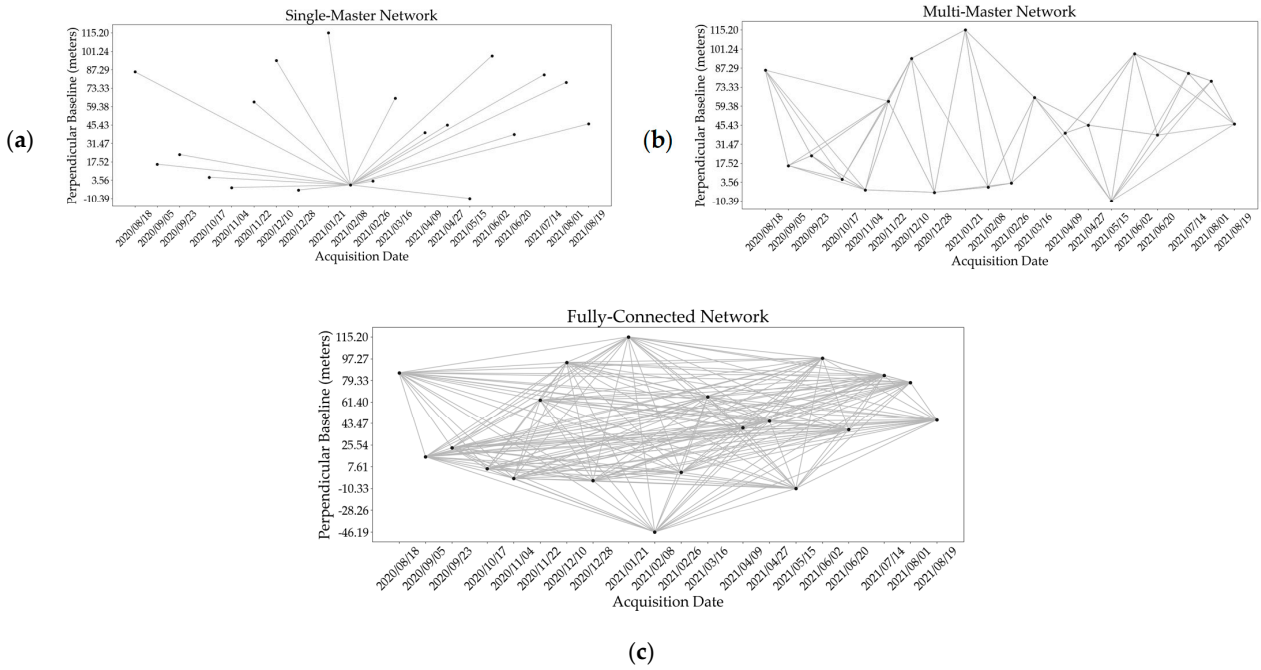


Figure 1. Visualization of different interferogram networks: (**a**) single-master network, (**b**) multi-master network, and (**c**) fully-connected network. The x-axis represents the acquisition date, while the y-axis represents the perpendicular baseline in meters.

While PSI methods can potentially provide highly accurate estimates, their effectiveness is limited in non-urban areas due to the scarcity of PS pixels, resulting in sparse measurement points. This sparsity presents challenges during the unwrapping process and in reducing the atmospheric effects. To overcome these limitations and extend the capability of deformation analysis to non-urban areas, the next generation of TSI methods relaxed the requirement of selecting only highly reflective points. Instead, they allowed the inclusion of points that could maintain an acceptable level of coherence in short-temporal interferograms. Unlike PS points, which typically correspond to a single highly reflective scatterer within a pixel, these new points, known as distributed scatterers (DS), represent groups of neighboring pixels that exhibit similar statistical behavior. Although these points are affected by signal decorrelation, if averaged, they can achieve a sufficient SNR, making them suitable for time-series analysis [5,9,10]. Methods that utilize DS points are gener-

ally referred to as distributed scatterer interferometry (DSI). The averaging techniques applied to DS pixels can involve multilooking, as seen in small baseline subset (SBAS) methods [3], or adaptive approaches that consider the statistical behavior of neighboring pixels [5,11–13]. Unlike PS, the interferogram network for DS pixels is not redundant because the averaging process disrupts the consistency among interferometric pairs. In practical terms, if n, m and q are three arbitrary epochs from the available data stack, Equation (1), known as phase triangularity [5,8], always holds true for PS pixels but does not apply to DS pixels [5,8,14,15]. As a result, these methods will have to deal with a multi-master interferogram network (Figure 1b).

$$\varphi_{m,q} = W[\varphi_{m,n} + \varphi_{n,q}] \quad (1)$$

where $\varphi_{m,q}$ is the interferometric phase between epochs m and q while W is the wrapping operator, indicating that the results are wrapped within the range $(-\pi, \pi)$. Since TSI analysis depends on a series of single-master consistent phase values, they must be extracted from the multi-master interferogram stack [8]. DSI methods approach this in two main ways. The first group of methods selects a subset of interferogram pairs with short temporal and/or spatial baselines. The SNR level of the subsets are then enhanced through multilooking, and finally, the single-master phase values are extracted from the unwrapped time-series phases of the available stack. This approach is mainly employed by SBAS methods [3]. The second approach involves creating a full stack of interferograms and extracting the single-master phases from the wrapped interferogram pairs after performing some form of averaging on the DS points. This approach is known as phase linking, as the estimated phases result from linking or jointly processing all available interferometric phases [2,5,6,8,16–19].

While PL methods require the creation of a fully-connected network of interferograms (Figure 1c), which can impose a significant computational burden, especially for studies conducted over long intervals, they have been proven to be highly effective in deriving consistent phases from interferometric stacks and significantly reducing the decorrelation noise [18]. Additionally, in [20], it was demonstrated that PL methods are capable of mitigating the phase bias aka fading signal. These signals are not present on PS points since they are the result of averaging on DS pixels, and they appear to have their strongest effects on short-term multilooked interferograms. Although the contribution of the phase bias is relatively small in a single interferogram compared to other sources such as deformation and elevation, their cumulative effect in methods that rely solely on short-term interferograms, like SBAS, can introduce biases in the estimated deformation [15,20]. In contrast, PL methods, which utilize all possible interferometric combinations and include long-term interferograms in their estimation process, are much less susceptible to these biases, making them highly reliable for time-series analysis [2,15,21]. Another significant advantage of PL methods is that they estimate the single-master phase series before the unwrapping stage, which greatly improves the quality of unwrapping, reduces the risk of unwrapping errors, and results in a more reliable time-series estimation [8]. PL methods are expected to produce a denser map than PSI methods due to the inclusion of DS points in the time-series analysis, and in contrast to SBAS methods, they are better at handling phase inconsistencies, leading to a higher SNR and more reliable single-master phase results from DS points.

Theoretically, PL methods based on maximum likelihood (ML) estimation are expected to produce results that are closest to the Cramér–Rao lower bound (CRLB), representing the lowest possible variance for an unbiased estimator [10]. This level of precision, however, depends on certain critical conditions being met. Firstly, a fully-connected network of interferograms, covering all possible combinations of temporal baselines, is required. Secondly, in the context of ML estimation, the method assumes an unbiased estimation of the coherence matrix, representing the correlation between different interferometric pairs [8,18].

In practice, meeting these conditions can be quite challenging, particularly in non-urban and vegetated areas. In these regions, high decorrelation leads to a sharp decrease

in coherence, even with small increases in the time interval between acquisitions. As a result, long-term interferograms for such areas often contain significant noise and exhibit coherence levels close to zero. Including these noisy interferograms in the network can be counterproductive, as it degrades the quality of the final results rather than enhancing them. Specifically, the noise in linked phases can lead to poor performance during the unwrapping stage, which is critical for accurate phase estimation and deformation monitoring. Another factor to consider is the potential challenges during interferogram generation such as poor SAR data acquisitions, faults in the orbital parameters, issues with coregistration, or gaps in monitoring that lead to data unavailability for certain regions during specific time periods. Additionally, systematic errors in the interferogram generation process can also prevent the successful creation of interferograms, further complicating the analysis.

Furthermore, the existence of systems like COMET-LiCSAR [22] or ARIA [23], which provide pre-generated interferograms for various parts of the Earth, offers significant benefits for large-scale monitoring and analysis. However, given the enormous amount of data generated due to the short revisit times of satellites like Sentinel-1, these systems often focus on creating interferograms with short temporal baselines. This practical approach means that a full stack of interferograms for every region might not be available, leading to an incomplete interferogram network. Consequently, it is important to understand how effectively PL methods can be applied to these pre-existing, incomplete networks, and to what extent the lack of data or the incompleteness of the interferogram network might impact the accuracy and reliability of the results. In this paper, we investigated the impact of the lack of interferograms in the interferogram network on the performance of PL methods across different land covers. For this analysis, we focused on two widely recognized PL methods, EVD [6,24,25] and EMI [2,26], which are favored for their high processing speed.

The rest of this paper is organized as follows. Section 2 provides a brief overview and explanation of the functioning of PL methods. In Section 3, we describe the various interferogram network configurations that will be examined to assess their effect on the results. Sections 4 and 5 detail the application of these network configurations to simulated and real data, respectively. Finally, in Section 6, we present the conclusions drawn from the study.

2. Materials and Methods

2.1. Sample Correlation Matrix

The extraction of single-master phases in most PL algorithms is based on the use of the complex sample covariance matrix or its normalized form, the complex sample correlation matrix (SCM) [2]. More precisely, the covariance matrix of an interferometric phase stack is essential for characterizing the statistical properties of DS pixels Therefore, in the following, a brief explanation will be given to familiarize the reader with the structure of this matrix and how different algorithms use it to obtain the single-master linked phases.

Based on the central limit theorem, SAR data vectors are assumed to follow a zero-mean, multi-dimensional, complex Gaussian probability distribution [27]. Therefore, to fully characterize the statistical properties of the data, it is essential to understand the covariance (or correlation) matrix. As demonstrated by [17], let $P = [p_1, p_2, \ldots, p_N]^T$ represent the vector of observed complex values for N SLC images for a group of neighborhood pixels represented as Ω, where p_m is a vector of size k, containing k samples (pixels) in the Ω for the arbitrary epoch m = 1, 2, . . ., N. The complex sample covariance matrix can be described as follows:

$$C = \frac{1}{k} \sum_{P \in \Omega} PP^H \tag{2}$$

If the observation vector is normalized, the complex SCM can also be demonstrated as:

$$\Gamma = \frac{1}{k} \sum_{\tilde{P} \in \Omega} \tilde{P}\tilde{P}^H \tag{3}$$

where $\tilde{P} = \left[\tilde{p}_1, \tilde{p}_2, \ldots, \tilde{p}_N\right]^T$ and $E\left[\left|\tilde{p}_i\right|^2\right] = 1$ and E is the expectation operator. Therefore, for the expanded version of SCM we have:

$$\Gamma = \begin{bmatrix} 1 & \gamma_{1,2} & \cdots & \gamma_{1,N-1} & \gamma_{1,N} \\ \gamma_{2,1} & 1 & & & \gamma_{2,N} \\ \vdots & & \ddots & & \vdots \\ \gamma_{N-1,1} & & & 1 & \gamma_{N-1,N} \\ \gamma_{N,1} & \gamma_{N,2} & \cdots & \gamma_{N,N-1} & 1 \end{bmatrix} \circ \begin{bmatrix} 0 & e^{j\phi_{1,2}} & \cdots & e^{j\phi_{1,N-1}} & e^{j\phi_{1,N}} \\ e^{j\phi_{2,1}} & 0 & & & e^{j\phi_{2,N}} \\ \vdots & & \ddots & & \vdots \\ e^{j\phi_{N-1,1}} & & & 0 & e^{j\phi_{N-1,N}} \\ e^{j\phi_{N,1}} & e^{j\phi_{N,2}} & \cdots & e^{j\phi_{N,N-1}} & 0 \end{bmatrix} \quad (4)$$

In this equation, $\gamma_{m,n}$ is the absolute value of the coherence and $\phi_{m,n}$ is the wrapped interferometric phase between two radar images m and n, respectively, and $\circ$ indicates elementwise matrix multiplication.

2.2. PL Methods

EVD, also known as CAESAR [6,17,25], offers unique capabilities compared to other methods. It is particularly effective in DSI for dealing with multiple scattering mechanisms. EVD can decompose the contributions of different scattering mechanisms, making it a powerful tool in this context. As provided by Equation (5), this method estimates the single-master linked phases by extracting the phases of the eigenvector associated with the largest eigenvalue of the complex sample covariance matrix or SCM, which basically represents the dominant scattering mechanism of the DS pixels. The key advantages of EVD in the context of PL methods is its computational efficiency. However, it is considered to be not as optimal for phase estimation as the ML-based method by [5] or EMI [2,26].

$$\Gamma\nu = \lambda_{max}\nu \quad (5)$$

where ν is the eigenvector associated with the largest eigenvalue extracted from SCM. The EMI method [2], compared to EVD and ML phase estimation by [5,18], offers both estimation optimality and computational efficiency. As shown in Equation (6), EMI also estimates the single-master time-series phase through eigenvalue decomposition, using the eigenvector corresponding to the minimum eigenvalue, and in comparison to the ML-based method by [5], it can improve the estimation efficiency, particularly when covariance or coherence estimation errors are present. While ML phase estimation can theoretically excel in estimation efficiency with high computational complexity and EVD is computationally efficient but less optimal in phase estimation, EMI combines the strengths of both, achieving efficiency and accuracy. In our implementation, we used the simplified version of EMI:

$$(|\Gamma|^{-1} \circ \Gamma)\nu = \lambda_{min}\nu \quad (6)$$

where $|\Gamma|$ is the estimated coherence matrix from SCM and ν is the eigenvector associated with the smallest eigenvalue extracted from the eigenvalue decomposition of $|\Gamma|^{-1} \circ \Gamma$.

3. Interferogram Network Configurations

Since in practice it may not be possible to have all the interferograms to implement PL methods, it might become necessary to use an almost dense or sparse SCM (in very extreme conditions) instead of a completely dense matrix. Due to this issue, we looked at the network of interferograms from the perspective of graph theory, in which case the coherence matrix ($|\Gamma|$) acts as an undirected graph whereas the phase matrix is a directed one. In these graphs, SAR acquisition represent the vertices and each edge, if available, represents the interferogram created by two arbitrary acquisitions (Figure 1). In order to understand the effect of the sparsity in the SCM (i.e., removing the edges of the interferograms network graph on the results of PL methods), EMI and EVD were implemented on the following three scenarios.

3.1. Banded Matrix Configuration

In this configuration, banded versions of the SCM matrix are used. These banded matrices are created based on putting a limit on temporal baselines, which is the conventional structure used in most SBAS methods. This approach is identical to the enhanced short temporal baseline subset (E-StBAS) method introduced by [20] when used with EVD. Therefore, the banded matrices are defined by a bandwidth parameter (bw), where only elements within a certain distance from the diagonal are retained. For example, if bw-3 is to be used, only the indices where $|m - n| \leq 3$ are included (Figure 2a).

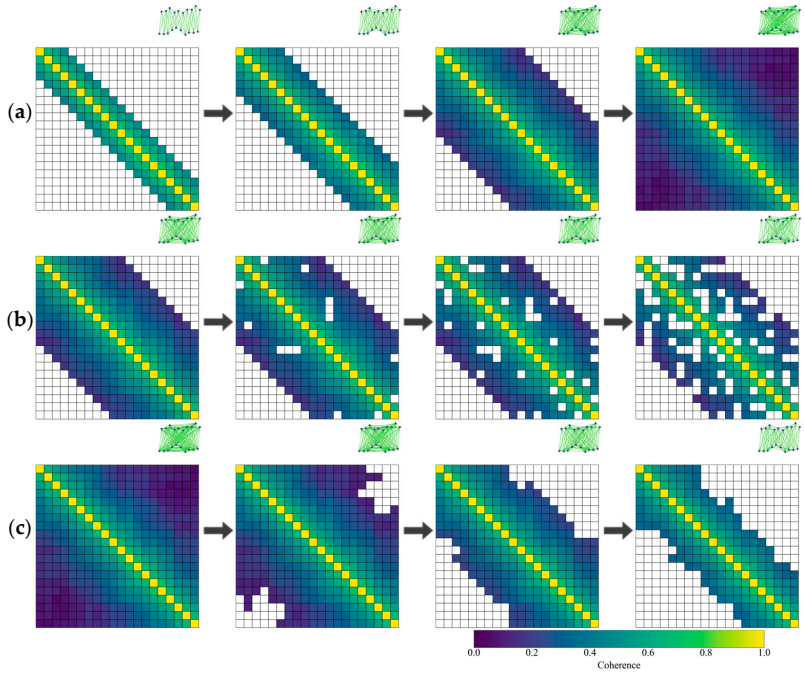


Figure 2. Visualization of the coherence matrix structures under different interferogram network configurations (with corresponding graphs on the top right of each matrix). Row (**a**) represents the banded matrix configuration, focusing on short temporal baselines. Row (**b**) shows the sparse matrix configuration, and row (**c**) presents the coherence thresholding configuration. White cells indicate the lack of interferograms or removed indices in the coherence and/or SCM matrix.

3.2. Sparse Matrix Configuration

In order to understand the effects of matrix sparsity in short temporal baselines on PL methods, we investigated the results by randomly removing SCM indices and gradually increasing the percentage of deleted cells (Figure 2b).

3.3. Coherence Thresholding Configuration

In this configuration, the SCM is filtered by applying a threshold to coherence values in the network of each individual pixel (Figure 2c). It is noteworthy to mention that in this scenario, a significant challenge might arise when applying thresholds to the SCM. This challenge involves maintaining network connectivity after applying a coherence threshold that might remove all the interferograms related to one epoch. To address this, we implemented an approach to ensure the robustness of the subsequent analysis. The initial step for the third scenario involves computing the absolute values of the SCM to obtain the coherence matrix. The threshold is then applied to filter out coherence values below a specified level (e.g., coherence < 0.3). While this thresholding procedure effectively removes the low coherence indices, it can also lead to an undesired graph disconnection in cases where the coherence values are low. In other words, if the resulting sparse matrix is interpreted as a graph, excessive thresholding may disconnect the graph, leaving some vertices (corresponding to SLC indices in the SCM or coherence matrix) isolated without

any edges. To mitigate this issue, we employed a minimum spanning tree (MST) approach on the upper triangle indices of the coherence matrix. By considering the inverted values of the coherence matrix as edge weights (i.e., using $1/|\Gamma|$ as costs), we ensured that the MST captured the optimal connectivity structure. This approach guarantees that the graph remains connected by identifying the most fundamental set of $N-1$ edges (for a graph with N nodes) that result in the minimum possible cost, thereby preserving the most coherent combination. Consequently, the indices (interferograms) corresponding to the edges selected by the MST are retained in the SCM, even after thresholding. This approach ensures that the connectivity of the graph is maintained, regardless of the threshold applied, thereby safeguarding the integrity of the PL analysis. An overview of all the structures of the SCM used in these three configurations can be seen in Figure 2.

4. Simulated Data Analysis

4.1. Simulation Settings

The performance of the EVD and EMI methods under three different interferogram network configurations was evaluated through the simulation of two different cases of the complex correlation matrix. Case A utilizes the temporal decorrelation model as described in [16], which is expressed as:

$$\Gamma_{m,n} = (\gamma_0 - \gamma_\infty)e^{-\frac{|\delta t_{m,n}|}{\tau}} + \gamma_\infty \tag{7}$$

In this model, $\gamma_0 = 0.6$ and $\gamma_\infty = 0.13$ represent the short-term decaying and long-term persistent coherence, respectively. The parameter $\delta t_{m,n}$ represents the temporal baseline between epochs m and n, while $\tau = 50$ days characterizes the temporal decorrelation constant (which represents the duration of signal correlation). This model effectively simulates the decaying coherence over time, offering valuable insights into the performance of PL techniques.

Case B extends the model to incorporate the systematic phase variations (phase bias) as outlined in [20], and is represented as:

$$\Gamma_{m,n} = \gamma_1 e^{-\frac{|\delta t_{m,n}|}{\tau_1}} e^{j\rho_{\phi 1}\Delta t} + \gamma_2 e^{-\frac{|\delta t_{m,n}|}{\tau_2}} e^{j\rho_{\phi 2}\delta t_{m,n}} + \gamma_\infty + (1 - (\gamma_1 + \gamma_2 + \gamma_\infty))\delta_{m,n}$$
$$\text{where } \delta_{m,n} = \begin{cases} 0 & \text{if } m \neq n. \\ 1 & \text{if } m = n \end{cases} \tag{8}$$

This extended temporal decorrelation model captures three key scattering behaviors that influence coherence over time: persistent coherence and two decorrelating components with distinct temporal constants. These components represent different physical scattering processes in the radar signal. The first scattering behavior is characterized by short-term coherence decay, modeled by $\gamma_1 = 0.18$ and a corresponding temporal constant of $\tau_1 = 11$ days. This short-term decay describes signals that lose coherence rapidly. The phase variation for this component is represented by $\rho_{\phi 1} = 0.03$ radian/day. The second scattering behavior represents long-term coherence decay, modeled by $\gamma_2 = 0.25$ with a longer temporal constant of $\tau_2 = 50$ days, accounting for slower decorrelation processes. The phase variation for this component is represented by $\rho_{\phi 2} = 0.002$ radian/day, indicating much slower phase evolution over time. Additionally, the model includes a persistent coherence term $\gamma_\infty = 0.13$, which accounts for a stable, long-term component that remains coherent regardless of time. Finally, $\delta_{m,n}$ is the Kronecker delta, ensuring that the coherence is properly handled for the same acquisitions (i.e., when $m = n$, the coherence equals 1). This term should not be confused with the temporal baseline $\delta t_{m,n}$, which represents the time difference between acquisitions. By separating these components, the model accurately simulates how coherence decays over time due to different physical processes, while the phase terms account for systematic phase variations that may lead to phase bias, especially in short-term interferograms. This helps explain the observed fading signals and short-lived phase behaviors in the radar data. In both cases, the target rate of displacement and

corresponding phases are intended to be zero. In Case A, this was true, while in Case B, a small phase bias was introduced in short-term interferograms to simulate systematic phase variations, though the overall rate of displacement remained close to zero.

To simulate conditions similar to those found in the DS points, by assuming 100 acquisitions with a 6 day interval between them, the two models were used to generate 100 noisy samples. These samples were then averaged to create an SCM, closely reflecting the behavior observed in real-world DS points.

By performing the EMI and EVD methods under different network configurations on these two models, a preliminary evaluation was conducted. This analysis will provide an initial understanding of the methods' behavior and offers valuable insights into the expected performance when these approaches are applied to real-world data.

4.2. Simulation Results

To account for the randomness of noise, 1000 realizations were performed for each case and configuration. The root mean square error (RMSE) was calculated by comparing the estimated single-master phase series results to those of the noise-free correlation matrix generated during the modeling step. For banded matrix configuration, bandwidths of three, five, and ten were tested and compared against a dense, fully-connected matrix. For the sparse matrix configuration, the SCM matrix with bw-10 was used as the base. The matrix was then sparsed randomly by removing 5%, 20%, and 40% of its elements. Results from these sparse matrices were compared to those of the bw-10 matrix to assess the performance degradation due to sparsity. As for the final configuration, thresholds of 0.1, 0.2, and 0.3 were applied to the SCM, and the performance of both methods on these modified matrices was then compared to the results obtained using the fully-connected matrix.

4.2.1. Case A

For the first network configuration, Figure 3a shows the performance of the EMI and EVD methods across different bandwidths, highlighting an improvement in RMSE when using lower bandwidths compared to the fully-connected network. Specifically, when smaller bandwidths (bw-3, 5, 10) were used, the methods resulted in lower RMSE values, indicating more precise estimates. In contrast, the fully-connected dense matrix that included all possible interferogram pairs produced the highest RMSE, representing the lowest performance. These results suggest that, in the absence of phase bias, focusing on short-term, high-coherence interferograms improves the estimation accuracy. This finding aligns with the underlying principles of the SBAS method, which prioritizes interferograms with shorter temporal baselines to achieve more reliable and accurate results.

For the second network configuration, Figure 3b shows that the RMSE for both methods increased as the level of sparsity in the interferogram network grew. However, the increase in RMSE was significantly greater for the EMI compared to the EVD. This issue, as noted in previous studies such as [8], is likely due to the reliance of ML methods, such as EMI, on the inversion of the coherence matrix, a process that is sensitive to numerical instabilities if the estimated coherence matrix is biased. In contrast, while EVD also experienced an increase in RMSE with higher sparsity, it remained more robust than EMI. This robustness stems from the fact that EVD does not depend on coherence matrix inversion (as shown in Equation (5)). Nevertheless, sparsity can still impact the EVD's performance, as the removal of matrix entries alters the spectral properties, such as eigenvalues and eigenvectors, disrupting the overall structure. These disruptions can introduce numerical instability and reduced accuracy, especially since eigenvalue decomposition is inherently more challenging for sparse matrices. To further verify the impact of coherence matrix sparsity on the EMI results, additional tests were conducted using the true coherence matrix and the estimated, not-sparsed coherence matrix for inversion. The results, presented in Figure 4, confirm that not only does a biased or sparse coherence matrix negatively affect EMI, but the increased sparsity further degrades its estimation quality. EVD, in contrast, remained more resilient to these conditions, demonstrating greater stability in sparse networks.

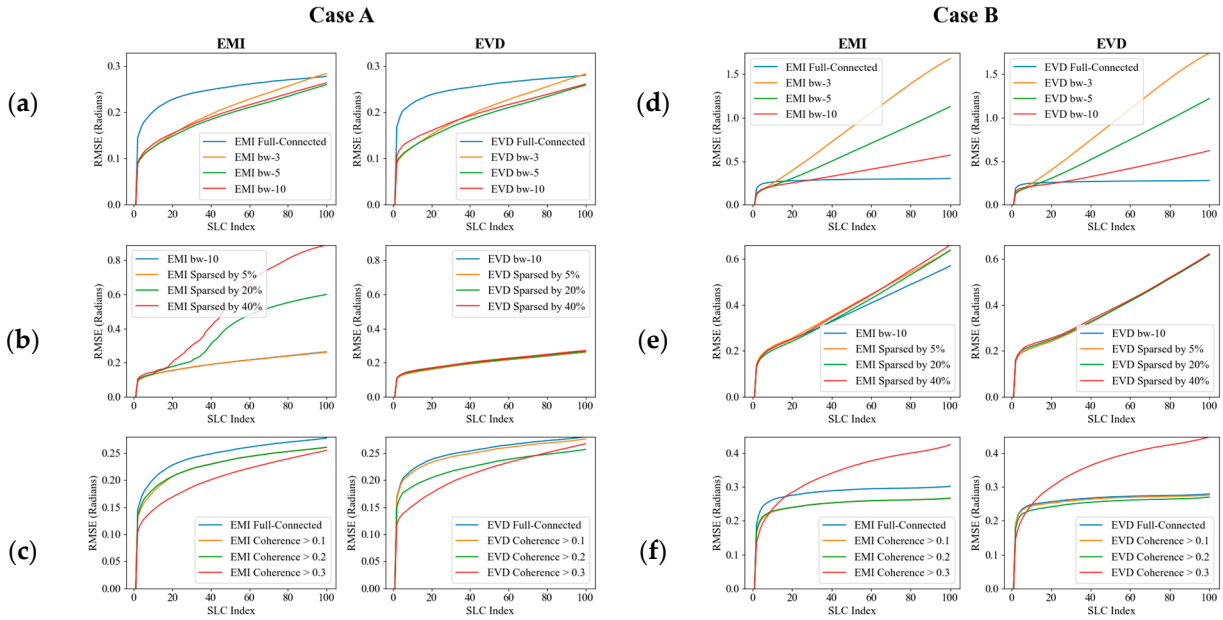


Figure 3. RMSE of the estimated single-master phase series results for both the EMI and EVD methods. Figures (**a**–**c**) correspond to Case A of the simulation, while figures (**d**–**f**) represent the results of Case B. Each figure displays two columns: the left column shows the results for EMI, and the right column shows the results for EVD.

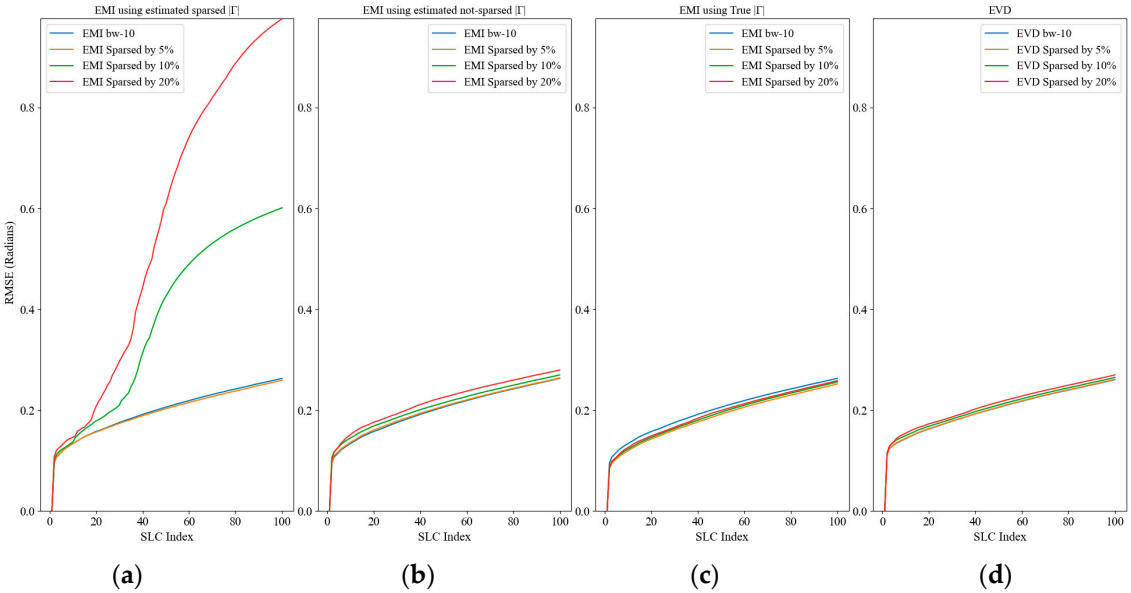


Figure 4. Comparison of RMSE for EMI and EVD under different coherence matrix configurations. (**a**) RMSE of EMI using a sparsed estimated coherence matrix from the banded sparse SCM for inversion. (**b**) RMSE of EMI using an estimated coherence matrix from the banded SCM without sparsity. (**c**) RMSE of EMI using the true but banded coherence matrix from the modeling step. (**d**) RMSE of EVD.

In the final network configuration, the results in Figure 3c show that applying thresholds, the same as using banded matrices, enhanced the performance of the methods. Specifically, the RMSE decreased as the threshold increased, indicating that removing low-coherence indices from the SCM matrix leads to more accurate estimates. EMI, in particular, showed considerable improvement as these lower-coherence elements were filtered out, suggesting that the method can benefit from excluding less reliable data.

4.2.2. Case B

In the first network configuration for Case B, the RMSE for both the EMI and EVD methods showed a marked decrease as the bandwidth of the matrices was increased. This is in contrast to the findings in Case A, where increasing bandwidth had the opposite effect. This observation aligns with the work of [20], which demonstrated similar results using the E-StBAS method on real data. The results suggest that excluding longer-term interferograms, such as in traditional SBAS methods, can lead to more errors due to the phase bias present in short-term multilooked interferograms. Since this phase bias is short-lived, using interferograms with longer temporal baselines (i.e., increasing the bandwidth) actually improves the estimation accuracy. This is evident in Figure 3d, where the RMSE for both the EMI and EVD methods significantly decreased as the bandwidth increased, indicating that the inclusion of longer-term data mitigates the impact of phase bias. To better illustrate the impact of phase bias on single-master phase series estimation and the resulting rate of displacement, additional figures, Figure 5a,b, are provided.

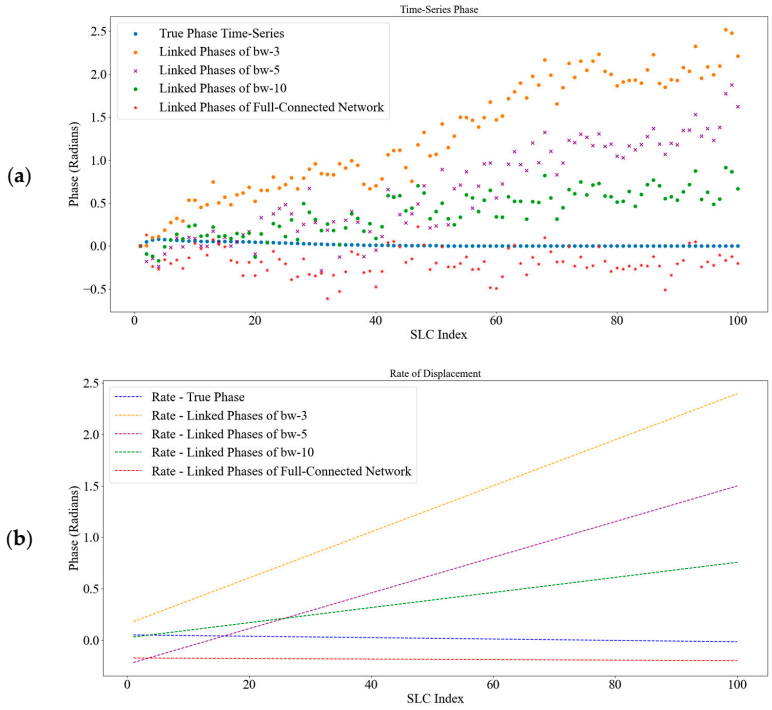


Figure 5. (**a**) Plot of the estimated single-master phase series values displaying five different series. The true phase series (blue), which remained nearly zero except for small values in the short-term indices simulating phase bias, was compared against four other series: resulting from bw-3, 5, 10, and the fully-connected network. As the bandwidth increased and more long-term interferograms were included, the estimated phase series results moved progressively closer to the true phase series. (**b**) The rate of displacement calculated from all five phase series, showing how even a small phase bias in the short-term interferograms resulted in a significant overestimation of the rate of displacement.

In the second configuration, similar to Case A, the estimation efficiency for both methods decreased as the sparsity percentage of the SCM matrix increased. The RMSE was increased as more elements were removed, with the EMI method being particularly more sensitive to this sparsity. As observed in Case A, the EVD method demonstrated greater robustness to sparsity, maintaining a relatively lower RMSE compared to EMI as the SCM became sparser (Figure 3e).

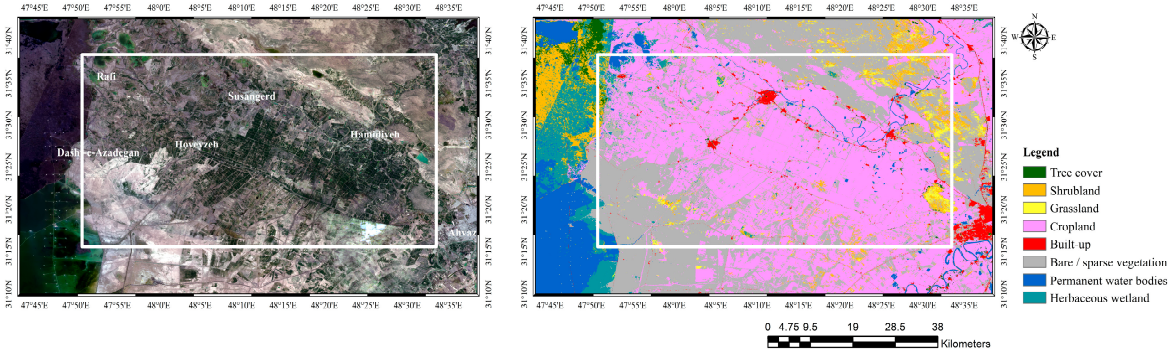
In the final configuration, a different pattern was seen compared to Case A. Initially, the RMSE improved when the low-coherence indices were filtered out using thresholds of 0.1 and 0.2, with 0.2 yielding the lowest RMSE for the single-master phase series in both the EMI and EVD methods (Figure 3f). However, when the threshold was raised to 0.3,

resulting in the removal of more indices, the RMSE increased significantly. This suggests that while filtering out low-coherence values can be beneficial in cases with phase bias (as in Case B), the excessive removal of data, especially of the long-term interferograms, can lead to over-reliance on short-term data. As observed in the first configuration, this reliance on short-term data introduces more errors due to the phase bias inherent in such data. Therefore, it is crucial to strike a balance when applying thresholds: removing enough low-coherence indices to improve accuracy without discarding so much data that the estimation becomes overly sensitive to phase bias.

5. Real Data Analysis

5.1. Study Area

We selected a study area in the southwest of Iran, characterized by a diverse range of land cover types including agricultural, urban, and bare landscapes (Figure 6). The area was monitored by Sentinel-1A and B satellites, with a total of 62 images acquired on track 108 between 18 August 2020 and 19 August 2021. All possible interferometric pairs were processed, resulting in 1891 interferograms generated using the TOPS stack processor package in the ISCE2 software (v2.6.3) [28]. Multilooking was applied by factors of 5 in the range and 20 in the azimuth directions, and geocoding was performed onto a 100 m grid using Shuttle Radar Topography Mission (SRTM) elevation data [29].



(**a**) (**b**)

Figure 6. Study area overview. (**a**) The study site is located in southwest Iran, west of the city of Ahvaz, with the boundaries of the area marked by the white polygon. The background imagery was sourced from USGS Landsat 8 Level 2, Collection 2, Tier 1 (LANDSAT/LC08/C02/T1_L2). (**b**) Land cover classification map of the study area, derived from Google Earth Engine using The European Space Agency (ESA) WorldCover 10 m 2020 land cover map product [30].

5.2. Real Data Results

5.2.1. Banded Matrix Configuration Results

For the first network configuration, in order to investigate the effects of using short temporal interferograms on different land cover types, various bandwidths (bw-3, 5, 15, 30, 45) were tested along with a fully-connected matrix to compare the performance of the EMI and EVD methods. The rate of displacement was calculated for each land cover type including built-up areas, cropland, and bare land using 100 adjacent pixels per type. The choice of 100 pixels was made to minimize the influence of localized anomalies while effectively capturing the overall displacement trends within these regions. The results were then analyzed to determine how different bandwidth choices affected the displacement measurements across these land cover types. It is important to note that the goodness-of-fit measure by [5] was applied throughout the analysis to ensure that only reliable pixels were considered, removing those with low temporal coherence from the PL methods' results. This measure can be written as:

$$\gamma = \frac{2}{N(N-1)} \sum_{m=1}^{N} \sum_{n=m+1}^{N} \cos\left(\Delta\phi_{m,n} - \hat{\phi}_n + \hat{\phi}_m\right) \quad (9)$$

where $\Delta\phi_{m,n}$ represents the original interferogram phase difference between acquisitions m and n, and $\hat{\phi}_m$,$\hat{\phi}_n$ are the corresponding estimated phases from PL. It is noteworthy to mention that the given formula is designed for a fully-connected matrix. In order to calculate this measure for any type of sparsified matrix, we used a slightly modified version:

$$\gamma = \frac{1}{M} \sum_{m=1}^{N} \sum_{n=m+1}^{N} \cos\left(\Delta\phi_{m,n} - \hat{\phi}_n + \hat{\phi}_m\right) \tag{10}$$

where M represents the number of available interferograms in the network.

As shown in Figure 7a, the rate of displacement revealed that using short temporal baselines led to overestimated displacement rates in most regions, likely due to phase bias. This issue gradually improved as the bandwidth increased for both the EMI and EVD methods. These observations aligned well with the findings of [20], where the E-StBAS approach was employed, which similarly benefited from higher bandwidths. Figure 7b–g illustrates the mean rate of displacement calculated from the 100 adjacent pixels for each land cover type. The rate of displacement across different land cover types revealed that phase bias had a significant impact on the estimation across all land covers. However, the extent of this impact varied, depending on the land cover type. The observed pattern of estimated rates and their improvement with increasing bandwidth closely mirrored the trends seen in the simulated data in Figure 5b, further confirming the benefits of including longer temporal baselines in reducing phase bias.

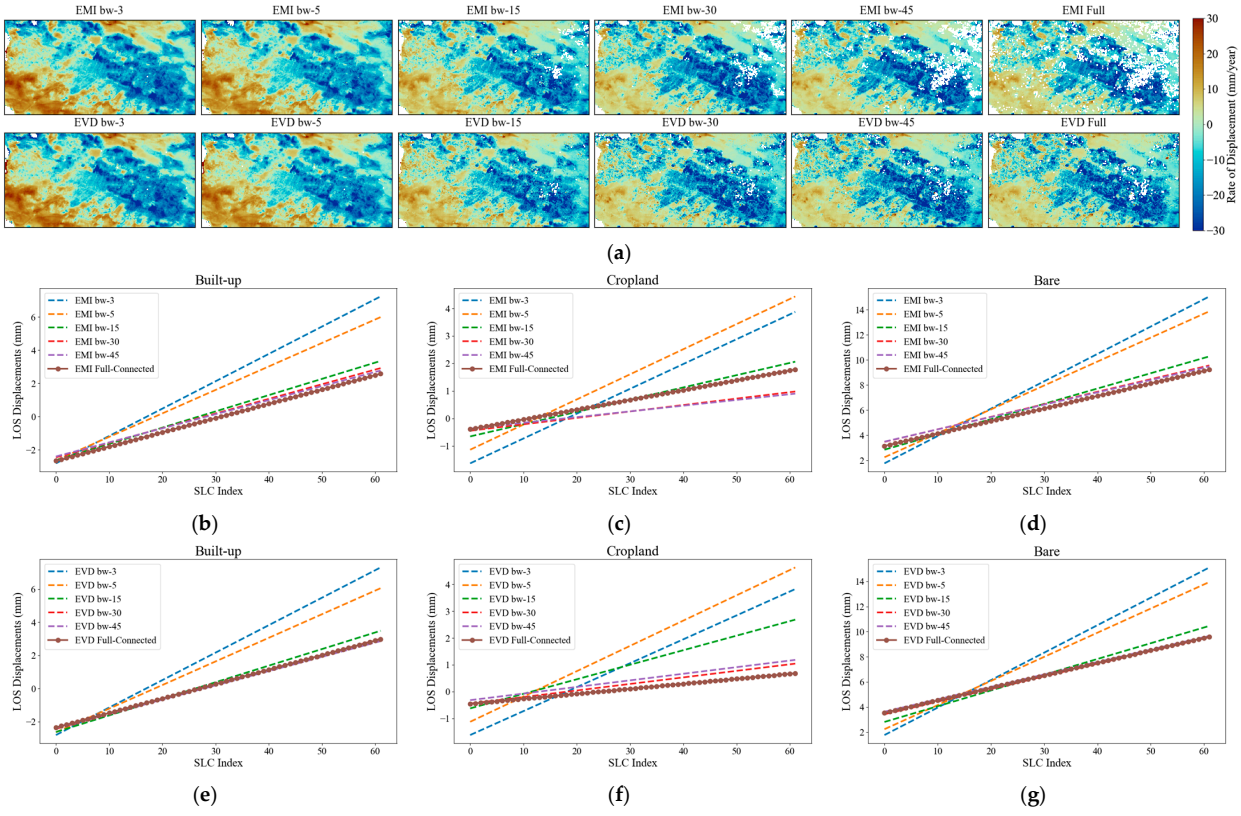


Figure 7. (**a**) Series of rate of displacement maps (in mm/year) for both the EMI and EVD results. The first row shows the rate of displacement for EMI, while the second row presents the results for EVD. Each column corresponds to a different banded network configuration: bandwidths of 3, 5, 15, 30, 45, and the fully-connected network, as indicated in the column titles. (**b**–**d**) The mean rate of displacement for EMI, calculated from the line of sight (LOS) cumulative displacements of 100 adjacent pixels for built-up areas, cropland, and bare land, respectively. (**e**–**g**) The same mean rate of displacement, calculated from cumulative displacements, but for the EVD results.

5.2.2. Sparse Matrix Configuration Results

To assess the impact of sparsity on short temporal baseline networks, three bandwidths (bw-5, 10, 15) were selected for evaluation. For each of these bandwidths, varying percentages of data (5%, 10%, 15%, 20%, 30%, 40%, and 50%) were randomly removed from the banded matrices to simulate different levels of sparsity. Histograms were generated for 300 pixels in each land cover type to compare the differences in displacement rates between the sparse network and the original banded network (without sparsity). By analyzing the standard deviation and mean values of these rate of displacement differences, the effect of sparsity on displacement estimation across different land cover types and temporal baselines was evaluated.

As illustrated in Figures 8 and 9, increasing sparsity negatively affected the accuracy of the results for both the EMI and EVD methods. The histograms generated for all land cover types demonstrated that as the percentage of sparsity increased, the accuracy of the displacement estimates declined. This was evident from the increasing standard deviation and shifts in the mean values of the histograms. While all land cover types were affected, built-up areas exhibited the greatest resilience, showing the lowest standard deviation values as the sparsity increased, indicating they are less sensitive to data loss. Bare land also showed moderate resilience while cropland was the most affected, with the highest standard deviation values under increasing sparsity.

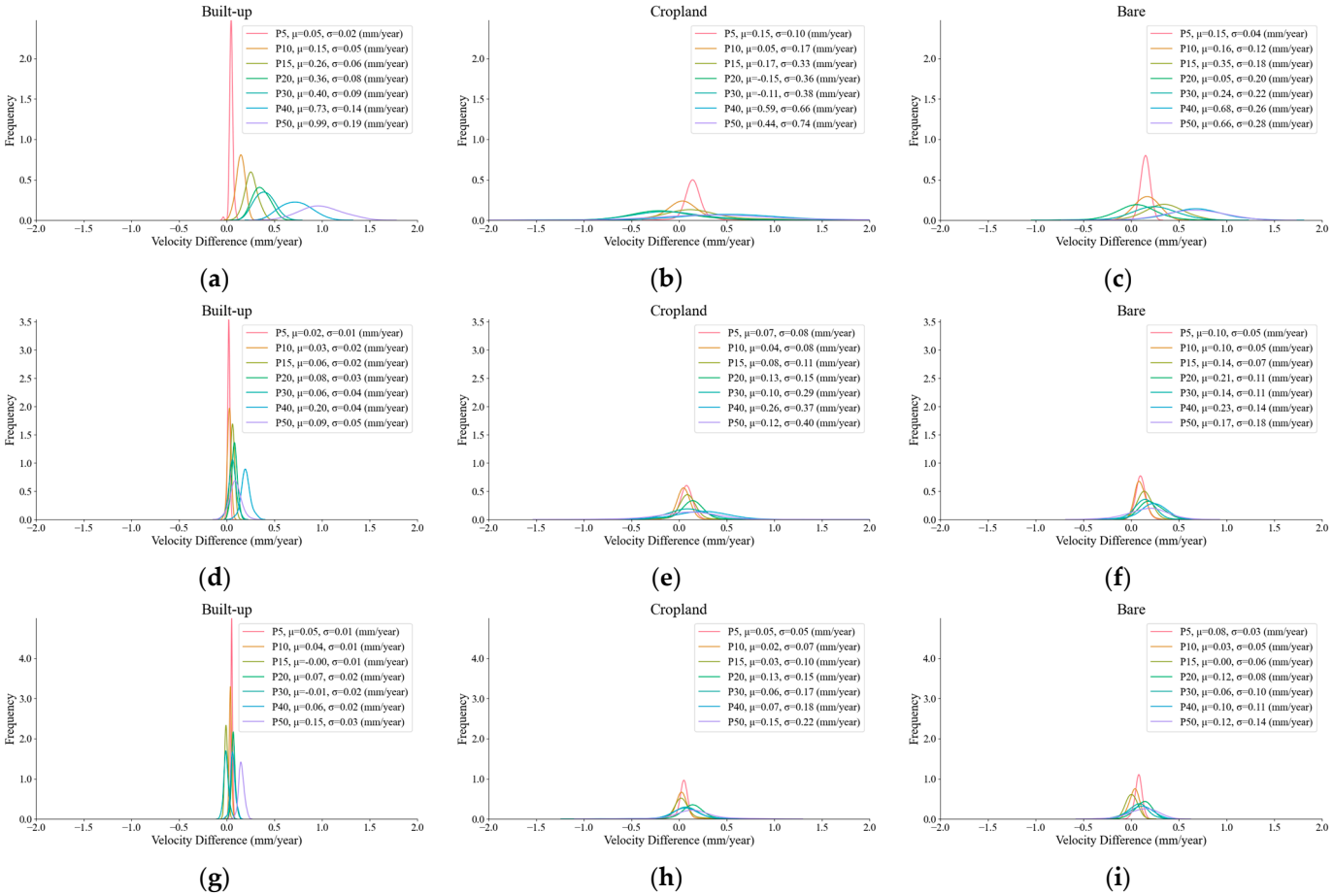


Figure 8. Histograms showing the differences between the rate of displacement for banded configurations (bw-5, 10, 15) and their respective sparsified networks at varying percentages for the EMI method. (**a**–**c**) Represent the differences between bw-5 and its sparsified versions across different land covers: built-up (**a**), cropland (**b**), and bare land (**c**). (**d**–**f**) Show the same structure for bw-10, and (**g**–**i**) for bw-15. Each plot includes the mean and standard deviation values of the histograms to highlight the impact of increasing sparsity on the rate of displacement estimation for each land cover type.

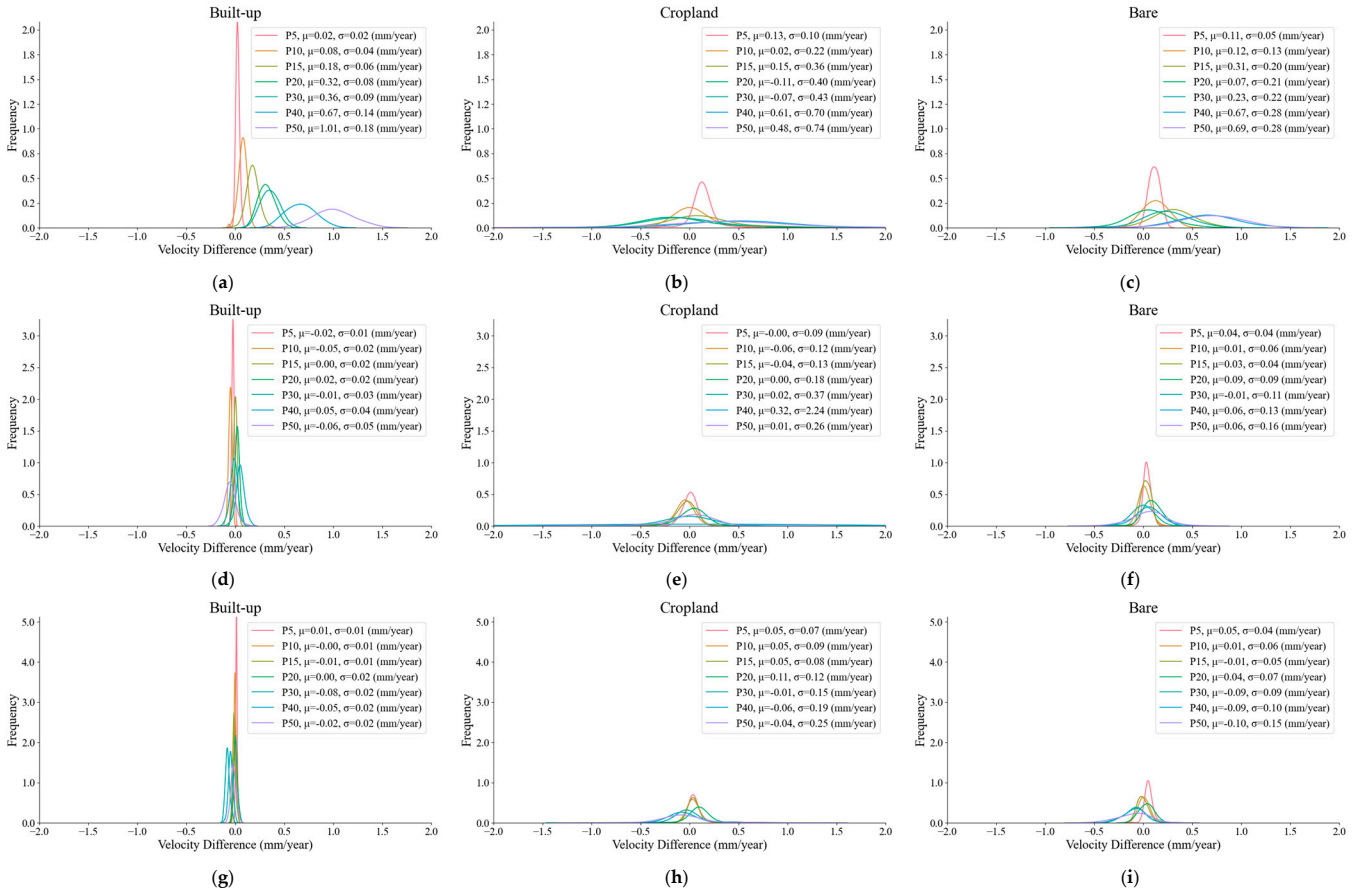


Figure 9. Histograms showing the differences between the rate of displacement for banded configurations (bw-5, 10, 15) and their respective sparsified networks at varying percentages for the EVD method. (**a**–**c**) Represent the differences between bw-5 and its sparsified versions across different land covers: built-up (**a**), cropland (**b**), and bare land (**c**). (**d**–**f**) Show the same structure for bw-10, and (**g**–**i**) for bw-15. Each plot includes the mean and standard deviation values of the histograms to highlight the impact of increasing sparsity on the displacement accuracy for each land cover type.

This trend suggests that built-up areas are more robust against the effects of data sparsity, while cropland is particularly sensitive to data loss. Additionally, the results align with the findings from simulated data, where EVD consistently outperforms EMI in sparse network conditions. EVD demonstrates lower standard deviation and mean values across different land cover types compared to EMI, indicating better robustness. It is also evident that higher bandwidths, especially bw-15 (Figures 8g–i and 9g–i), are less affected by sparsity for both methods. In contrast, lower bandwidths, such as bw-10 and bw-5, show greater sensitivity to increasing sparsity. This indicates that increasing the bandwidth can help mitigate the negative effects of sparsity, improving the stability and accuracy of displacement estimates to some extent.

5.2.3. Coherence Thresholding Configuration Results

In the final scenario, coherence thresholds of 0.4 and 0.5 were applied to evaluate their impact on the performance of the EMI and EVD methods. These thresholds were chosen to assess how removing low-coherence interferograms affected the quality of the results, particularly in terms of noise reduction and accuracy. For clearer visualization, the analysis focused on a subset of the study area, where one of the 6-day interferograms reconstructed by the phase linking methods is presented (Figures 10a–c and 11a–c). In addition, velocity (rate of displacement) maps for this region, generated using various thresholds, are provided to compare the outcomes (Figures 10d–f and 11d–f). The evaluation also

included two important quality parameters: the velocity standard deviation (VSTD) and spatio-temporal consistency (STC) employed by [31], which offer a more comprehensive assessment of the effects of different thresholds on the overall data quality and consistency across different land cover types (Table 1).

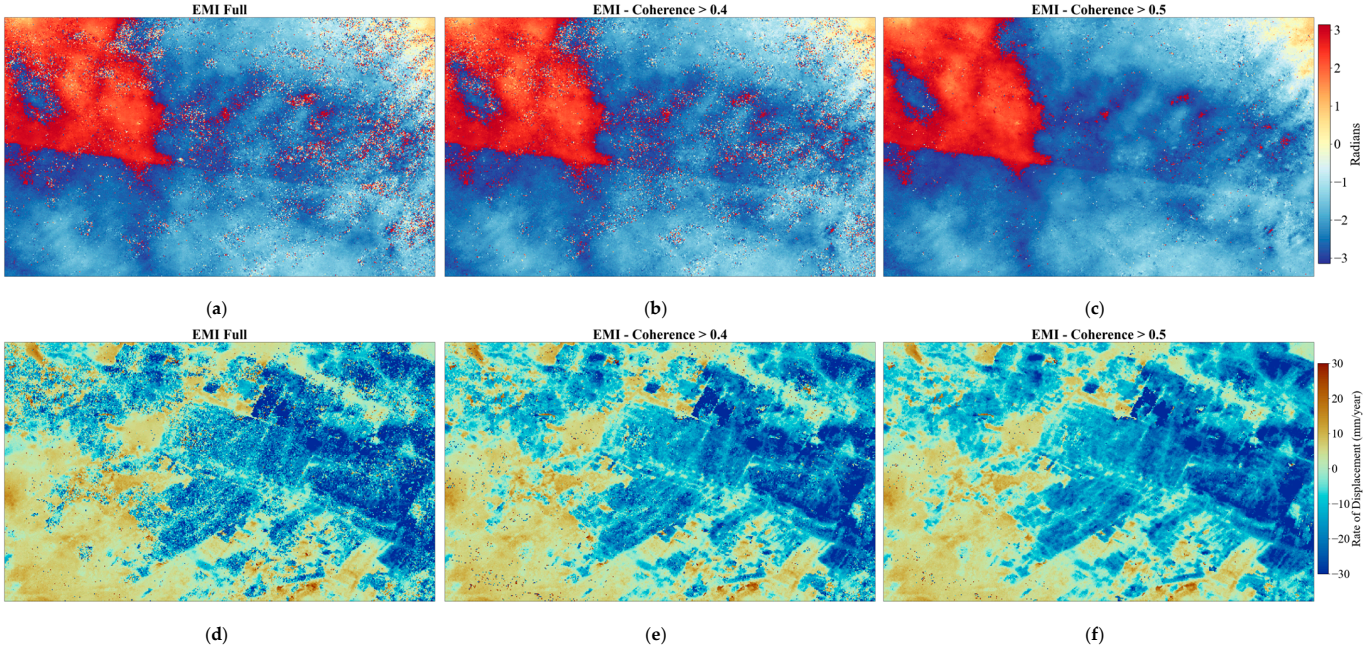


Figure 10. (**a**–**c**) Reconstructed interferograms of one of the original 6-day interferograms using the linked phase results from EMI, and (**d**–**f**) the corresponding velocity maps derived from the different interferogram networks. (**a**,**d**) Represent the results from the fully-connected network, while (**b**,**e**) are the results by applying a coherence threshold of 0.4, and (**c**,**f**) used a threshold of 0.5.

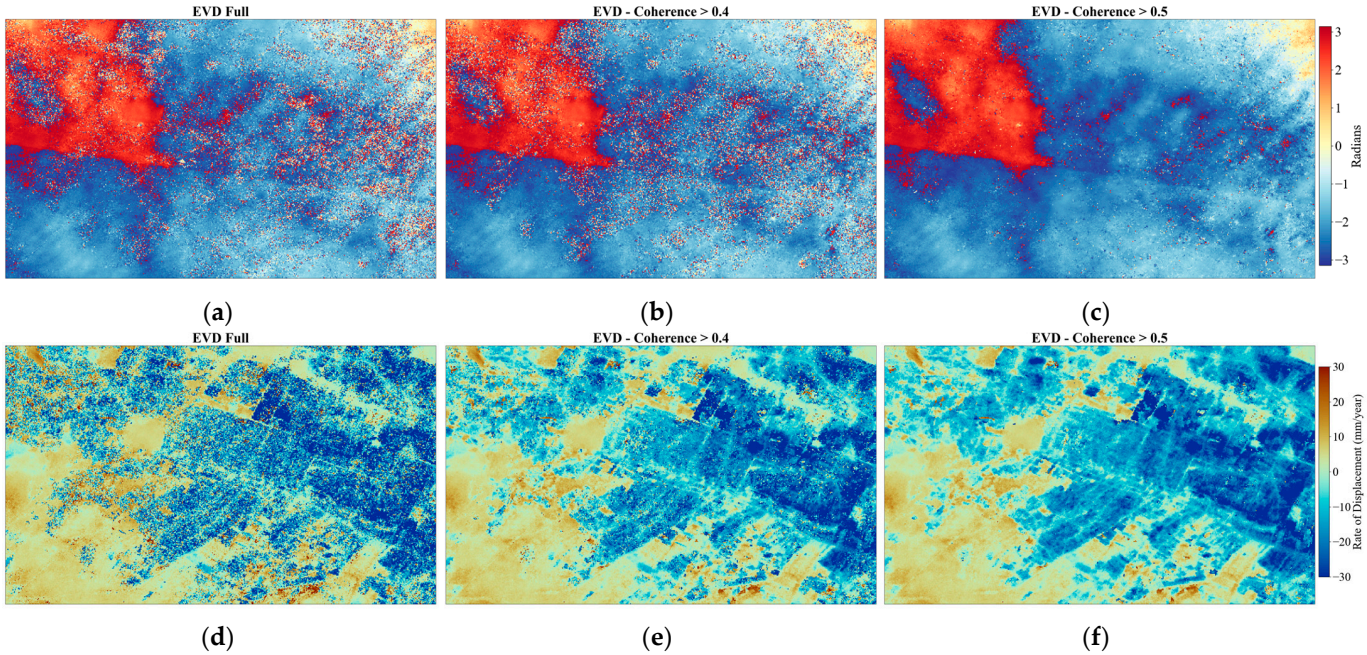


Figure 11. (**a**–**c**) Reconstructed interferograms of one of the original 6-day interferograms using the linked phase results from EVD, and (**d**–**f**) the corresponding velocity maps derived from the different interferogram networks. (**a**,**d**) represent the results from the fully-connected network, while (**b**,**e**) are the results by applying a coherence threshold of 0.4, and (**c**,**f**) used a threshold of 0.5.

Table 1. Quality parameters, VSTD and STC, across different land cover types for the EMI results under various interferogram network configurations.

STC				VSTD			
Network Configuration	**Built-Up**	**Cropland**	**Bare**	**Network Configuration**	**Built-Up**	**Cropland**	**Bare**
Fully-Connected	0.35	2.50	0.43	Fully-Connected	2.13	2.90	8.44
$\|\Gamma\| > 0.4$	0.42	1.63	0.42	$\|\Gamma\| > 0.4$	2.18	2.32	8.44
$\|\Gamma\| > 0.5$	0.40	0.87	0.39	$\|\Gamma\| > 0.5$	2.09	2.03	8.37

The application of coherence thresholds led to notable improvements in both methods, with the EMI results showing significant enhancements. As demonstrated in Figure 10a–c, the EMI results improved considerably as higher thresholds were applied, resulting in reconstructed interferograms that became progressively less noisy. This reduction in noise contributed to better unwrapping and overall smoother outputs. The estimated rate of displacement maps in Figure 10d–f reinforced this trend, showing that the exclusion of low-coherence interferograms led to more reliable displacement estimates while also mitigating the effects of phase bias. The EVD method also showed improvements in both the reconstructed wrapped interferograms (Figure 11a–c) and the estimated velocity maps (Figure 11d–f), although the EMI results were noticeably smoother, aligning with the patterns observed in the simulated data.

The use of VSTD and STC allowed for a detailed comparison of how coherence thresholding affected the data quality. As shown in Tables 1 and 2, both the VSTD and STC values decreased as the coherence threshold increased, reflecting a reduction in noise and an overall improvement in data quality. This trend was particularly evident in cropland areas, where the removal of noisy interferograms significantly enhanced the quality of displacement estimates. While the improvements in bare and built-up land covers were less pronounced, cropland benefited greatly from the higher thresholds, as removing low-coherence indices substantially enhanced the reliability of the results. Based on visual interpretation and quality parameters analysis, EMI generally outperformed EVD, especially in cropland areas, where it provided higher quality displacement estimates. However, EMI showed a slight decrease in quality in built-up areas and an even smaller impact in bare land. This suggests that in highly coherent networks such as those in built-up areas, the disadvantages of introducing sparsity outweigh the benefits of removing low-coherence indices. EVD, in contrast, remained more robust, showing little to no difference in performance after the removal of low-coherence interferograms and being less affected by sparsity than EMI in these land covers. These findings indicate that a constant coherence threshold may not always be beneficial. In highly coherent areas like built-up land covers, removing indices can introduce unnecessary sparsity, potentially harming data quality, even if the effect is small. However, in land covers like cropland, coherence thresholding can significantly improve results by enhancing the quality of the estimates.

Table 2. Quality parameters, VSTD and STC, across different land cover types for the EVD results under various interferogram network configurations.

STC				VSTD			
Network Configuration	**Built-Up**	**Cropland**	**Bare**	**Network Configuration**	**Built-Up**	**Cropland**	**Bare**
Fully-Connected	0.26	3.24	0.61	Fully-Connected	2.04	3.37	8.35
$\|\Gamma\| > 0.4$	0.26	2.14	0.48	$\|\Gamma\| > 0.4$	2.04	2.58	8.34
$\|\Gamma\| > 0.5$	0.26	1.10	0.44	$\|\Gamma\| > 0.5$	2.04	2.09	8.35

6. Conclusions

While PL methods like EMI and EVD have been traditionally designed for use on the full network of interferograms, the results demonstrate that they can be effectively applied to networks with short temporal baselines. These methods excel at extracting

coherent signals from the available data stacks, which leads to the creation of higher-quality reconstructed interferograms. This, in turn, can reduce the occurrence of unwrapping errors, while also offering the advantage of not having to unwrap all available interferograms. However, the success of these methods remains closely tied to the structure of the interferogram network on which they are applied.

When short temporal baselines are predominantly used, as explored through the application of different bandwidths, the results produced by these methods are generally smoother and exhibit less noise. However, this approach introduces a significant challenge by increasing the susceptibility of the methods to phase bias. Phase bias can have a substantial impact on the accuracy of the results, often leading to an overestimation of the displacement rates, which undermines the reliability of the findings.

Filtering out low-coherence interferograms, which are typically associated with longer temporal baselines, can significantly enhance the quality of the results, particularly by reducing noise. Nevertheless, two important considerations must be taken into account. First, the excessive removal of low-coherence interferograms by applying high threshold levels can cause the methods to become overly dependent on short temporal data. Although this process reduces noise, short-term data are more susceptible to phase bias, and an over-reliance on it can lead to less accurate estimates despite the noise reduction. Second, setting high thresholds can result in a sparse coherence matrix, especially in highly decorrelating regions where coherence levels are hard to maintain. The degree of sparsity introduced by these thresholds can lead to errors when applying PL methods. The extent to which this sparsity affects the results depends on the specific characteristics of the study area and the structure of the interferogram network being used.

In conclusion, both the choice of thresholds for the coherence level and the selection of bandwidths are critical decisions that must be tailored to the specific conditions of the study area. There is no one-size-fits-all solution; instead, these parameters must be carefully adjusted based on the unique characteristics of each case to optimize the performance of the EMI and EVD methods.

Author Contributions: Conceptualization, S.H.S.; methodology, S.H.S. and Y.M.; software, S.H.S. and Y.M.; validation, S.H.S. and Y.M.; formal analysis, S.H.S.; investigation, S.H.S. and Y.M.; writing—original draft preparation, S.H.S.; writing—review and editing, S.H.S. and Y.M.; visualization, S.H.S.; supervision, Y.M.; project administration, Y.M. All authors have read and agreed to the published version of the manuscript.

Funding: This research received no external funding.

Data Availability Statement: The data underlying this article will be shared on reasonable request to the corresponding author.

Acknowledgments: The Sentinel-1 data used in this research was provided by the European Space Agency (ESA). The Interferometric Synthetic Aperture Radar Scientific Computing Environment (ISCE) was used to generate the complete stack of interferograms.

Conflicts of Interest: The authors declare no conflicts of interest.

References

1. Ferretti, A.; Prati, C.; Rocca, F. *Non-Uniform Motion Monitoring Using the Permanent Scatterers Technique*; European Space Agency, (Special Publication) ESA SP: Strasbourg, France, 2000; pp. 431–436.
2. Ansari, H.; De Zan, F.; Bamler, R. Efficient Phase Estimation for Interferogram Stacks. *IEEE Trans. Geosci. Remote Sens.* **2018**, *56*, 4109–4125. [CrossRef]
3. Berardino, P.; Fornaro, G.; Lanari, R.; Sansosti, E. A New Algorithm for Surface Deformation Monitoring Based on Small Baseline Differential SAR Interferograms. *IEEE Trans. Geosci. Remote Sens.* **2002**, *40*, 2375–2383. [CrossRef]
4. Ferretti, A.; Prati, C.; Rocca, F. Nonlinear Subsidence Rate Estimation Using Permanent Scatterers in Differential SAR Interferometry. *IEEE Trans. Geosci. Remote Sens.* **2000**, *38*, 2202–2212. [CrossRef]
5. Ferretti, A.; Fumagalli, A.; Novali, F.; Prati, C.; Rocca, F.; Rucci, A. A New Algorithm for Processing Interferometric Data-Stacks: SqueeSAR. *IEEE T. Geosci. Remote Sens.* **2011**, *49*, 3460–3470. [CrossRef]

6. Fornaro, G.; Verde, S.; Reale, D.; Pauciullo, A. CAESAR: An Approach Based on Covariance Matrix Decomposition to Improve Multibaseline–Multitemporal Interferometric SAR Processing. *IEEE Trans. Geosci. Remote Sens.* **2015**, *53*, 2050–2065. [CrossRef]
7. Hooper, A.; Zebker, H.; Segall, P.; Kampes, B. A New Method for Measuring Deformation on Volcanoes and Other Natural Terrains Using InSAR Persistent Scatterers. *Geophyiscal Res. Lett.* **2004**, *31*. [CrossRef]
8. Samiei Esfahany, S.; Martins, J.; Van Leijen, F.; Hanssen, R. Phase Estimation for Distributed Scatterers in InSAR Stacks Using Integer Least Squares Estimation. *IEEE Trans. Geosci. Remote Sens.* **2016**, *54*, 5671–5687. [CrossRef]
9. Zebker, H.A.; Villasenor, J. Decorrelation in Interferometric Radar Echoes. *IEEE Trans. Geosci. Remote Sens.* **1992**, *30*, 950–959. [CrossRef]
10. Rocca, F. Modeling Interferogram Stacks. *Geosci. Remote Sens. IEEE Trans.* **2007**, *45*, 3289–3299. [CrossRef]
11. Goel, K.; Adam, N. A Distributed Scatterer Interferometry Approach for Precision Monitoring of Known Surface Deformation Phenomena. *Geosci. Remote Sens. IEEE Trans.* **2014**, *52*, 5454–5468. [CrossRef]
12. Parizzi, A.; Brcic, R. Adaptive InSAR Stack Multilooking Exploiting Amplitude Statistics: A Comparison Between Different Techniques and Practical Results. *IEEE Geosci. Remote Sens. Lett.* **2011**, *8*, 441–445. [CrossRef]
13. Shamshiri, R.; Nahavandchi, H.; Motagh, M.; Hooper, A. Efficient Ground Surface Displacement Monitoring Using Sentinel-1 Data: Integrating Distributed Scatterers (DS) Identified Using Two-Sample t-Test with Persistent Scatterers (PS). *Remote Sens.* **2018**, *10*, 794. [CrossRef]
14. Zheng, Y.; Fattahi, H.; Agram, P.; Simons, M.; Rosen, P. On Closure Phase and Systematic Bias in Multilooked SAR Interferometry. *IEEE Trans. Geosci. Remote Sens.* **2022**, *60*, 1–11. [CrossRef]
15. Maghsoudi, Y.; Hooper, A.J.; Wright, T.J.; Lazecky, M.; Ansari, H. Characterizing and Correcting Phase Biases in Short-Term, Multilooked Interferograms. *Remote Sens. Environ.* **2022**, *275*, 113022. [CrossRef]
16. Mirzaee, S.; Amelung, F.; Fattahi, H. Non-Linear Phase Linking Using Joined Distributed and Persistent Scatterers. *Comput. Geosci.* **2023**, *171*, 105291. [CrossRef]
17. Cao, N.; Lee, H.; Jung, H.C. Mathematical Framework for Phase-Triangulation Algorithms in Distributed-Scatterer Interferometry. *IEEE Geosci. Remote Sens. Lett.* **2015**, *12*, 1838–1842. [CrossRef]
18. Guarnieri, A.M.; Tebaldini, S. On the Exploitation of Target Statistics for SAR Interferometry Applications. *IEEE Trans. Geosci. Remote Sens.* **2008**, *46*, 3436–3443. [CrossRef]
19. Ansari, H.; De Zan, F.; Bamler, R. Sequential Estimator: Toward Efficient InSAR Time Series Analysis. *IEEE Trans. Geosci. Remote Sens.* **2017**, *55*, 5637–5652. [CrossRef]
20. Ansari, H.; De Zan, F.; Parizzi, A. Study of Systematic Bias in Measuring Surface Deformation With SAR Interferometry. *IEEE Trans. Geosci. Remote Sens.* **2021**, *59*, 1285–1301. [CrossRef]
21. De Zan, F.; Zonno, M.; Lopez Dekker, P. Phase Inconsistencies and Multiple Scattering in SAR Interferometry. *Geosci. Remote Sens. IEEE Trans.* **2015**, *53*, 6608–6616. [CrossRef]
22. Lazecký, M.; Spaans, K.; González, P.J.; Maghsoudi, Y.; Morishita, Y.; Albino, F.; Elliott, J.; Greenall, N.; Hatton, E.; Hooper, A.; et al. LiCSAR: An Automatic InSAR Tool for Measuring and Monitoring Tectonic and Volcanic Activity. *Remote Sens.* **2020**, *12*, 2430. [CrossRef]
23. Buzzanga, B.; Bekaert, D.; Hamlington, B.; Sangha, S. Toward Sustained Monitoring of Subsidence at the Coast Using InSAR and GPS: An Application in Hampton Roads, Virginia. *Geophys. Res. Lett.* **2020**, *47*, e2020GL090013. [CrossRef]
24. Verde, S.; Reale, D.; Pauciullo, A.; Fornaro, G. Improved Small Baseline Processing by Means of CAESAR Eigen-Interferograms Decomposition. *ISPRS J. Photogramm. Remote Sens.* **2018**, *139*, 1–13. [CrossRef]
25. Cao, N.; Lee, H.; Jung, H.C. A Phase-Decomposition-Based PSInSAR Processing Method. *IEEE Trans. Geosci. Remote Sens.* **2016**, *54*, 1074–1090. [CrossRef]
26. Ansari, H.; De Zan, F.; Gomba, G.; Bamler, R. EMI: Efficient Temporal Phase Estimation and Its Impact on High-Precision InSAR Time Series Analysis. In Proceedings of the IGARSS 2019—2019 IEEE International Geoscience and Remote Sensing Symposium, Yokohama, Japan, 28 July–2 August 2019; pp. 270–273. [CrossRef]
27. Bamler, R.; Hartl, P. Synthetic Aperture Radar Interferometry. *Inverse Probl.* **1998**, *14*, 4. [CrossRef]
28. Fattahi, H.; Agram, P.; Simons, M. A Network-Based Enhanced Spectral Diversity Approach for TOPS Time-Series Analysis. *IEEE Trans. Geosci. Remote Sens.* **2016**, *55*, 777–786. [CrossRef]
29. Farr, T.; Rosen, P.; Caro, E.; Crippen, R.; Duren, R.; Hensley, S.; Kobrick, M.; Paller, M.; Rodriguez, E.; Roth, L.; et al. The Shuttle Radar Topography Mission. *Rev. Geophys.* **2007**, *45*, RG2004. [CrossRef]
30. Zanaga, D.; Van De Kerchove, R.; De Keersmaecker, W.; Souverijns, N.; Brockmann, C.; Quast, R.; Wevers, J.; Grosu, A.; Paccini, A.; Vergnaud, S.; et al. ESA WorldCover 10 m 2020 V100 2021. [CrossRef]
31. Morishita, Y.; Lazecky, M.; Wright, T.J.; Weiss, J.R.; Elliott, J.R.; Hooper, A. LiCSBAS: An Open-Source InSAR Time Series Analysis Package Integrated with the LiCSAR Automated Sentinel-1 InSAR Processor. *Remote Sens.* **2020**, *12*, 424. [CrossRef]

Disclaimer/Publisher's Note: The statements, opinions and data contained in all publications are solely those of the individual author(s) and contributor(s) and not of MDPI and/or the editor(s). MDPI and/or the editor(s) disclaim responsibility for any injury to people or property resulting from any ideas, methods, instructions or products referred to in the content.